THE ASTROPHYSICAL JOURNAL LETTERS, 945:L33 (8pp), 2023 March 10 https://doi.org/10.3847/2041-8213/acbe00

Determining the IBEX Ribbon Transverse Profile from ENA Temporal Variations: A Proof of Concept for IMAP Observations

M. A. Dayeh[1,2], E. J. Zirnstein[3], and D. J. McComas[3]
[1] Southwest Research Institute, San Antonio, TX 78238, USA; maldayeh@swri.edu
[2] University of Texas at San Antonio, San Antonio, TX 78249, USA
[3] Department of Astrophysical Sciences, Princeton University, Princeton, NJ 08544, USA

Received 2022 November 13; revised 2023 February 8; accepted 2023 February 21; published 2023 March 14

Abstract

Since its discovery in 2009, the IBEX energetic neutral atom (ENA) Ribbon has been a subject of numerous studies. It appears at energies ∼0.5–6 keV and is most pronounced at ∼1–3 keV. It is almost circular, ∼20°–40° wide, and its center lies near the pristine local interstellar magnetic field direction, whose field lines are draped around the heliosphere. The Ribbon intensity is enhanced above the more diffuse, globally distributed flux (GDF) and varies on timescales that are delayed compared to the underlying and slowly varying GDF. We present a novel method to infer the Ribbon boundaries and transverse profile of the Ribbon using sequential time variations of ENA fluxes, with minimal modeling assumptions involved. The method utilizes the difference in temporal evolution between the total Ribbon content and GDF fluxes. We then use the inferred Ribbon transverse profile to statistically quantify the GDF contribution to the observed peak Ribbon intensity to be ∼32.23% ± 3.15% in 2009–2011. This Ribbon separation method works best during times of gradual changes in solar wind output, and with high angular resolution and ENA counting statistics; results thus provide a proof of concept for the upcoming Interstellar Mapping and Acceleration Probe ENA measurements.

Unified Astronomy Thesaurus concepts: Heliosphere (711); Heliosheath (710); Pickup ions (1239); Interstellar magnetic fields (845); Solar wind (1534); Solar cycle (1487)

1. Introduction

Over the six months after its launch in 2008, The Interstellar Boundary EXplorer (IBEX; McComas et al. 2009a) discovered a band of enhanced energetic neutral atom (ENA) emissions in the sky that are ∼2–3 times above the underlying globally distributed flux (GDF), dubbed the IBEX Ribbon (McComas et al. 2009b). The Ribbon has an average width of ∼20° FWHM (Fuselier et al. 2009) and is nearly circular in shape (Funsten et al. 2009) with an average radius of $74\overset{\circ}{.}81 \pm 0\overset{\circ}{.}65$ over all energies and is centered on ecliptic (J2000) coordinates [$218\overset{\circ}{.}33 \pm 0\overset{\circ}{.}68$, $40\overset{\circ}{.}38 \pm 0\overset{\circ}{.}88$] (Dayeh et al. 2019, see also Funsten et al. 2013). The IBEX Ribbon appears to be ordered by the interstellar magnetic field, having its center approximately aligned with the direction satisfying $B \cdot R \sim 0$ (Schwadron et al. 2009), where B is the local interstellar medium (LISM) magnetic field (ISMF) that is draped externally around the heliopause, and R is the radial line-of-sight view from the inner heliosphere (i.e., IBEX's boresight). The ENA flux distributions along the Ribbon in the sky are symmetric at ∼ 1 keV about the solar equatorial plane and exhibit a bimodal symmetry at higher energies (Funsten et al. 2015). The Ribbon center in the sky is distinct for each energy, with these centers aligned near the plane connecting the presumed ISMF direction and the interstellar gas inflow direction (the $B-V$ plane), and the variable SW structure along the heliographic meridian (Dayeh et al. 2019; Swaczyna et al. 2019). Numerous theories have been suggested to explain the source of the Ribbon (see McComas et al. 2009b, 2014), with the most prevailing being the "Secondary ENA mechanism," supported by several lines of evidence from observations and simulations (e.g., McComas et al. 2009b; Heerikhuisen et al. 2010; Möbius et al. 2013; Schwadron & McComas 2013; McComas et al. 2014; Zirnstein et al. 2015; Giacalone & Jokipii 2015; Zirnstein et al. 2016a; Swaczyna et al. 2016; McComas et al. 2017; Zirnstein et al. 2017; McComas et al. 2019; Dayeh et al. 2019). In the secondary ENA mechanism, interstellar neutrals penetrating into the heliosphere charge exchange with the supersonic SW ions to create "primary" ENAs. Some of these ENAs travel into the outer heliosheath and undergo two sequential charge exchange events: an ionization followed typically 2–3 yr later by another neutralization, creating "secondary" ENAs. The direction of motion of these secondary ENAs and the location of their origin are critical for understanding observations made at 1 au (e.g., Heerikhuisen et al. 2010; Zirnstein et al. 2015, 2016b).

Numerous studies have shown that the Ribbon sources are different from the GDF, which is mostly generated in the inner heliosheath (e.g., McComas et al. 2009b; Heerikhuisen et al. 2010; Schwadron et al. 2011; Möbius et al. 2013; Zirnstein et al. 2015; Giacalone & Jokipii 2015; Zirnstein et al. 2021 and references therein). However, the GDF may also make contributions to the secondary ENA process, generated outside the heliopause (e.g., Izmodenov et al. 2009; Opher et al. 2013; Zirnstein et al. 2014, 2019). This further emphasizes the need to separate these two populations across the sky. Nonetheless, separating the Ribbon from its underlying GDF is not a trivial task, given that ENAs observed at 1 au are an integrated accumulation along each IBEX pixel line of sight. The overlapping of source emission structures introduces ambiguity in the properties of the individual sources and their relative contributions that is not easy to pinpoint. As a result, basic assumptions about ENA sources may need to be made. Furthermore, low statistics in some directions of the sky introduce other challenges where the signal-to-noise ratio is low, e.g., where the Ribbon extends to high latitudes with lower intensity, and where it passes through the region when the Earth's magnetosphere is in IBEX's field of view (e.g., McComas et al. 2013, Dayeh et al. 2015).

Ribbon-GDF source separation has important implications. Ribbon-only fluxes would enable us to understand the nature and extent of the ISMF draping around the heliopause, thus providing direct information about the geometry of the heliosphere and the pristine LISM properties. Furthermore, Ribbon and GDF separation would enable us to better understand the GDF evolution across the sky, in particular, estimating the line-of-sight pressure, which is directly related to the thickness of the heliosheath and the parent ion distribution. In a series of papers, Schwadron et al. (2011, 2014, 2018) devised a method to separate the Ribbon from the GDF for three different time periods of the IBEX observations (2, 5, and 9 yr respectively). The authors used a transparency mask that suppresses enhanced fluxes (e.g., Ribbon) and used an interpolation scheme that filled in the resulting masked regions with interpolated ENA levels (Schwadron et al. 2011). One of their key results (Schwadron et al. 2014) is the construction of an all-sky map of line-of-sight integrated pressure. These maps showed a suprathermal pressure enhancement that is deflected ~20° south of the interstellar upwind direction. The deflection is consistent with the effects of the ISMF asymmetric draping around the heliopause and the nonradial flows observed by Voyager 2, further asserting that the pressure from suprathermal ions observed by IBEX plays a fundamental role in the pressure balance throughout the heliosheath (McComas and Schwadron et al. 2014). Schwadron et al. (2018) determined that the separated Ribbon ENA fluxes evolve at a different timescale than those of the GDF, with a time lag that is consistent with the generation of ions retained for several years beyond the heliopause. These observations provided further support to the secondary ENA source of the Ribbon.

Funsten et al. (2013) modeled the Ribbon and the slowly varying GDF using a statistical Bayesian framework in which the modeled quantities are statistically constrained by their observed variability over the entire sky. This enabled these authors to derive a spatial coherence parameter that characterized the spatial uniformity of the Ribbon. Reisenfeld et al. (2021) presented a method in which they performed temporal and spatial averaging of the Ribbon regions into megapixels to enhance statistics, and then fit it with a combination of nonlinear functions, such as a Gaussian or a second-order polynomial. Similar nonlinear fitting methods were also used earlier by other authors to infer the geometrical properties of the Ribbon (e.g., Zirnstein et al. 2016b; Dayeh et al. 2019; Swaczyna et al. 2019). Most recently, Swaczyna et al. (2022) utilized spherical harmonics to reproduce the GDF signal in directions away from the Ribbon and used this method to fill in the GDF behind the Ribbon. The authors constructed GDF-only maps and identified the direction of the maximum plasma pressure to be within the $B-V$ plane, at $\sim 17\overset{\circ}{.}2 \pm 0\overset{\circ}{.}5$ away from the upwind direction. These authors also subtracted the spherical harmonic fit GDF fluxes from the actual ENA data to provide Ribbon-only flux maps.

This work develops a different approach and demonstrates that the Ribbon transverse profile can be inferred using sequential time variations of ENA data with minimal modeling assumptions involved. The method interestingly enables us to derive asymmetric Ribbon transverse profiles for different directions in the sky. These profiles are then used to statistically quantify the GDF contributions to the total ENA fluxes of the Ribbon. We find that over all directions during 2009–2011, the GDF contributes by about $32.23\% \pm 3.15\%$ to the observed total Ribbon intensity at ~1.1 keV. The upcoming Interstellar Mapping and Acceleration Probe (IMAP) mission (McComas et al. 2018b) will provide high-resolution spatial and temporal ENA measurements. This method is a proof of concept that works better with the improved IMAP observations. The rest of the paper is organized as follows. Section 2 describes the data and methodology of Ribbon separation, demonstrating the ribbon variability in the sky and data assumptions, Section 3 presents the results, and Section 4 discusses the implications and the conclusions.

2. Data and Methodology

2.1. Data

Throughout this analysis, we use ENA fluxes from the IBEX-Hi instrument (Funsten et al. 2009b). Data come from validated data release #16 (McComas et al. 2020) and is survival probability-corrected in the RAM direction (i.e., when IBEX is ramming into ENAs) at the energy passband centered on ~1.1 keV. The Ribbon appears brightest at this energy channel. In principle, sequential variations of ENAs used in the forthcoming method could be back-to-back maps; but to improve statistics from IBEX-Hi measurements, we opted to use averages of annual groups that are separated by a few years, reflecting a significant change in the Ribbon fluxes over time, and minimal change in the surrounding GDF, such that the Ribbon transverse profile is more pronounced. This averaging approach has been used previously for analysis purposes to improve statistics (e.g., Zirnstein et al. 2017; Dayeh et al. 2019, 2022; Schwadron & McComas 2019; McComas et al. 2020). Here we average the data over two different groups of years; namely, years 2009, 2010, and 2011 (hereafter P1) and years 2014 and 2015 (hereafter P2), respectively. ENA fluxes did not significantly change throughout these periods, thus allowing us to statistically average them, but fluxes did change between P1 and P2. Interestingly, as we show in Section 3, this ~4 yr gap in time between P1 and P2 resulted in a significant decrease in the ~1.1 keV Ribbon fluxes, but less change in the ~1.1 keV GDF. Time-dependent modeling results from Zirnstein et al. (2020) suggest a significant decrease in the observed ~1.1 keV Ribbon flux occurs after 2012 due to a change in the neutralized SW speed. We also note that the most significant changes in the GDF are observed at the highest-energy channels (>2 keV; McComas et al. 2018a, 2019, 2020). Therefore, the unique evolution of ~1.1 keV ENA fluxes between these two particular time periods are chosen for our analysis.

2.2. Variability in the IBEX Ribbon and Data Assumptions

Figures 1(a) and (b) show the ENA fluxes at ~1.1 keV in the Ribbon-frame, centered on ecliptic latitude $219\overset{\circ}{.}72 \pm 0\overset{\circ}{.}95$ and ecliptic longitude $41\overset{\circ}{.}50 \pm 0\overset{\circ}{.}87$ (Dayeh et al. 2019) for the time periods P1 and P2. The Ribbon has clearly decreased in intensity from P1 to P2. Figure 1(c) shows the difference, *P1 – P2*, where the Ribbon distinctly stands out (in blue). Using this absolute difference, we devise a method to determine the Ribbon "boundaries" (defined as the regions where the ribbon

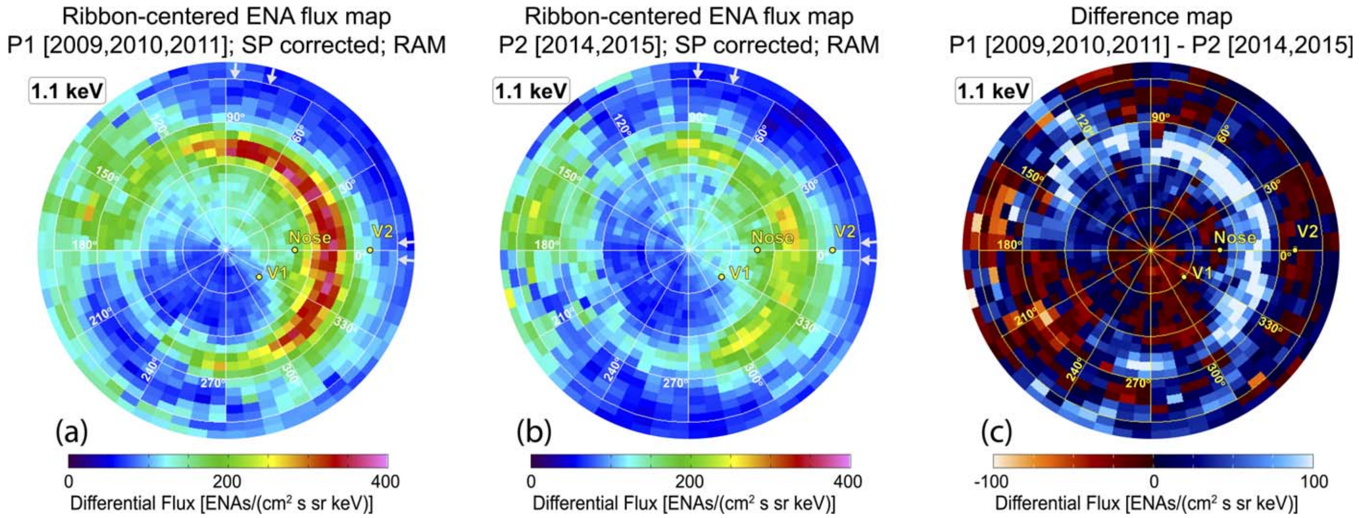

Figure 1. Time-averaged, Ribbon-frame maps of ENA fluxes at 1.1 keV during (a) period 1 (P1; 2009–2011 and (b) period 2 (P2; 2014–2015). (c) Difference flux maps showing the apparent evolution of the Ribbon fluxes. Gray arrows on the grid pointing inward mark the azimuths used for transverse profiles in Figure 2.

fluxes start to monotonically increase above the GDF) and estimate the underlying GDF for each azimuthal angle around the Ribbon center. In this plotting format, azimuths run from $0^{\rm o}$ to $360^{\rm o}$ in the counterclockwise direction, with the nose being at $0^{\rm o}$. Figure 1(c) further highlights that the evolution of the Ribbon in the sky is not uniform. This uneven change is likely coming from a combination of the independently varying GDF and Ribbon ENAs, with the latter having a higher contribution to Figure 1(c) given that the GDF is more stable over this particular time period, as we will show in Figure 2.

Figure 2 shows the variability of ENA fluxes for particular polar cuts at four azimuthal angles, indicated by gray arrows in Figure 1. Figure 2 shows transverse cuts of the Ribbon ENA fluxes along the polar angle during P1 (green) and P2 (blue), and their difference (red) at $3^{\rm o}$, $75^{\rm o}$, $87^{\rm o}$, and $357^{\rm o}$. The red curve reflects the rate of change of both the Ribbon and the surrounding GDF. The highly varying shape of the difference plot is clearly visible in the Ribbon region. A flat-top in panel (a) indicates a uniform change in ENA fluxes across the Ribbon; panels (b) and (c) show respectively a right- and left-skewed change in the Ribbon flux and panel (d) shows a change in the Ribbon flux that is approximately symmetric about the Ribbon's peak. Note that these asymmetric changes may also be a direct consequence of uneven variability in the neutral SW source in different directions of the sky, and not necessarily in the long-term averaged Ribbon transverse profile, especially if the cross section of the Ribbon transverse profiles in Figure 2 varies significantly in heliolatitude. Nonetheless, these observations emphasize that the Ribbon cannot be fit by a universal function that works for all times and directions in the sky; this is especially important considering that the Ribbon width is defined by roughly ∼8 pixels or less, which puts serious constraints on the number of parameters a model could have.

Driven by the variability in the total Ribbon signal, the Ribbon-GDF separation method developed in this work adapts two assumptions to the ENA data. The assumptions are based on previous Ribbon studies and are supported by observational evidence, as follows.

I. Compared to the Ribbon, we assume that the GDF varies slowly and smoothly as a function of time across the entire sky, including underneath the Ribbon, before the large increase in SW pressure in late 2014 and the reflected change in ENA fluxes in late 2016 (McComas et al. 2018a). This assumption is supported by GDF observations and that the Ribbon fluxes have much larger spatial gradients than the GDF (e.g., McComas et al. 2009a; Schwadron et al. 2014).

II. For a particular azimuthal sector, we assume that neutral SW flux evolves at the same rate in each 6°x6° pixel across the width of the Ribbon (FWHM $\sim 20^\circ$). This assumption is partially supported by the fact that the SW dynamic pressure, a significant contributor to the evolution of the neutral SW, is largely latitude invariant (McComas et al. 2008), but may be sensitive to strong changes in SW speed, which appears to significantly affect the Ribbon at ∼1 keV (Zirnstein et al. 2020). The SW dynamic pressure is not expected to vary significantly with longitude, except in cases of solar transients. Moreover, this assumption applies to each Ribbon transverse profile separately, which is $\sim 6^\circ$x20° in size, where the profile slice is "tilted" with respect to the solar equatorial plane at different angles along the Ribbon. We expect this assumption has the largest uncertainties when the profile extends over large a large range of latitudes. However, this only occurs at low latitudes. At high latitudes, the profile is more parallel to the equatorial plane, and thus less affected by switches between slow and fast SW. Note that this assumption is inherently adopted by all ribbon-fitting methods that model the ribbon as a mathematical function.

Aside from assumptions I and II, the presented method does not adopt further modeling assumptions, including interpolations across the Ribbon gap using any Ribbon information.

2.3. Ribbon Separation Methodology

Throughout this analysis, several azimuth directions were excluded for different reasons: (i) directions where uncertainties in ENA fluxes exceeded the actual flux values (4 swaths); (ii) directions where the magnetospheric obstacle is located, this is characterized by low statistics and high noise dominance (18 swaths); (iii) azimuths in the downwind directions, this

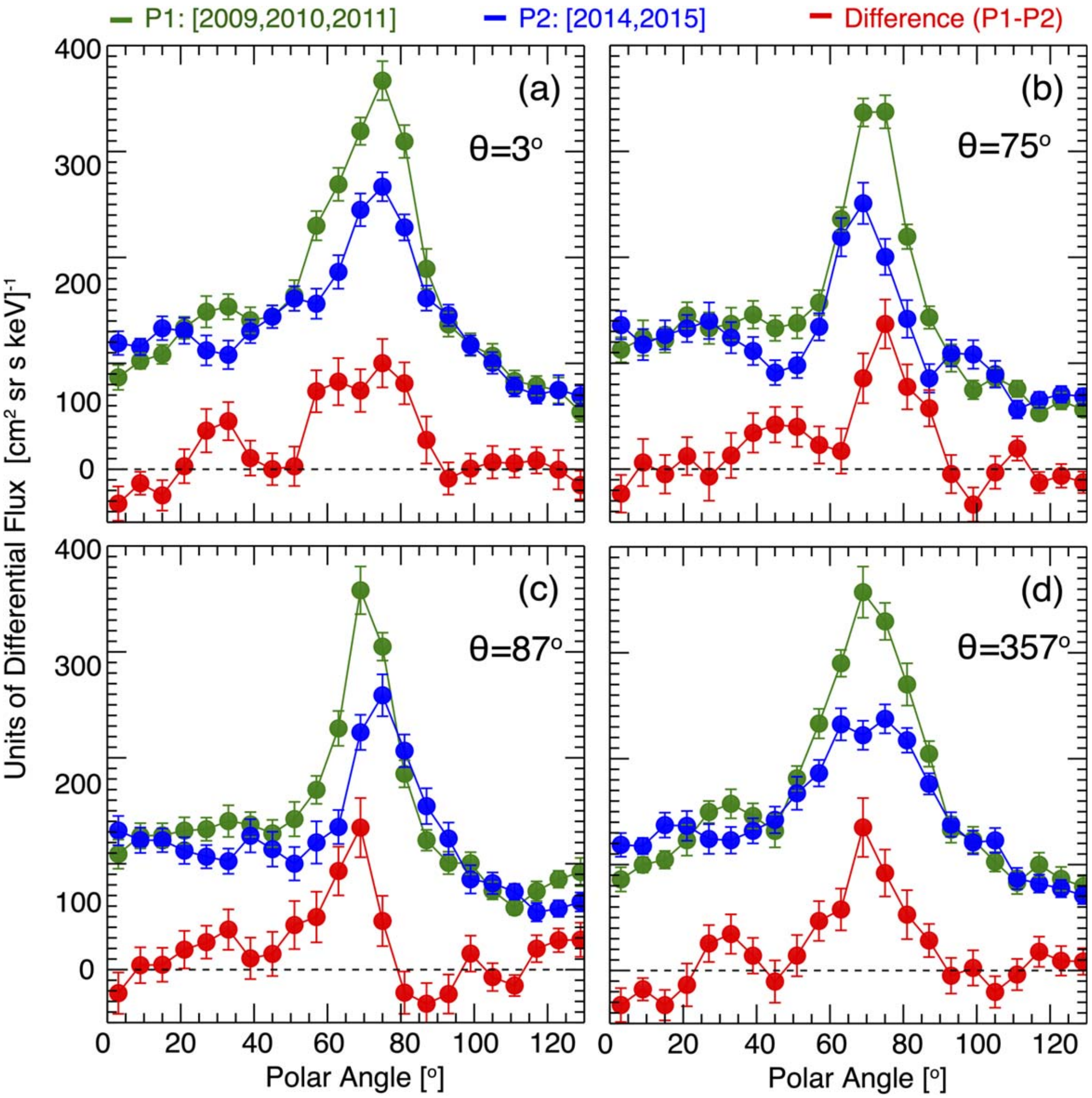

Figure 2. ENA fluxes during the time periods P1 (green) and P2 (blue) studied here, along with their difference (red) for four different Ribbon transverse profiles (see gray arrows in Figures 1(a) and (b)). The figure highlights the distinctive transverse profiles that the Ribbon and its evolution over time could take. (a) shows a relatively symmetric flux change rate across the Ribbon; (b) and (c) show a one-sided skewed change and (d) shows a symmetric rate of change.

region partly overlaps with the magnetospheric region and the Ribbon fluxes are less certain (6 swaths); and (iv) azimuths where Ribbon flux values in both time periods are too similar, leading to a difference flux that is within the surrounding GDF fluctuations and preventing the determination of the Ribbon boundaries from the difference of fluxes (4 swaths). This exclusion process leaves 28 swaths for further analysis.

Figure 3 demonstrates the full process of our analysis. Figure 3(a) shows ENA fluxes from P1 and P2 in a particular azimuth in the sky (315°). In this particular cross section of the Ribbon, the Ribbon flux significantly decreases over time (from P1 to P2) while the GDF appears to vary slowly as a function of time, at least outside the main Ribbon region (assumption I). The lack of abrupt changes of the GDF outside the Ribbon also implies similar behavior inside the Ribbon (assumption I). We determine the transverse profile and relative contribution of the Ribbon flux in this example data set. The methodology of determining the Ribbon transverse profile is described in the following three main steps.

(1) *Ribbon boundaries.* Illustrated in Figure 3(b). Ribbon boundaries are the polar angles within which the Ribbon is pronounced and dominates the ENA signal. We start from the maximum flux difference, often located near the Ribbon peak flux, and track this difference down in both directions of the polar angle away from the peak until a “near-GDF” level is detected. The “near-GDF” level is defined when the difference flux reaches its closest approach to the zero level (red dotted line). These boundaries can also be determined with other statistical techniques and generally yield similar results.

(2) *GDF level estimation*. Once the Ribbon boundaries are determined, we now estimate a likely GDF profile for each azimuth on a case-by-case basis. The method is illustrated in Figure 3(c). In all ribbon separation studies to date, efforts generally adopted an interpolation scheme that bridged the GDF gap underneath the ribbon, based on the measured GDF levels around it. Here we adapt a different approach in which the GDF under the ribbon is inferred from the ribbon region fluctuations during the consecutive time periods. Measured

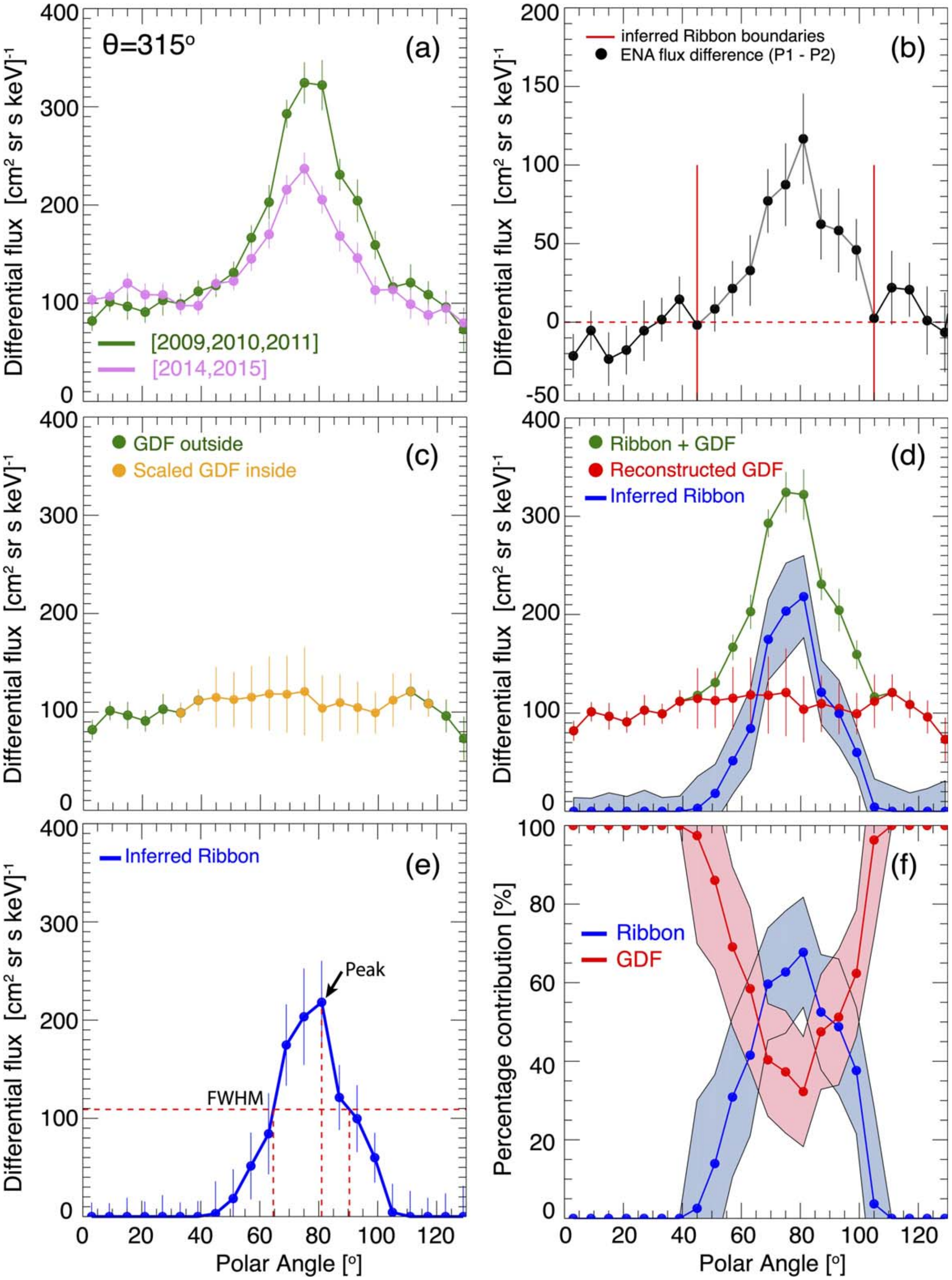

Figure 3. (a) Azimuthal cut of the Ribbon at 315^{o} azimuth showing the averaged ENA fluxes at 1.1 keV for P1 and P2. (b) Ribbon flux differences using data from (a); Red horizontal line marks the zero line of the difference flux, and vertical lines mark inferred Ribbon boundaries closest to the zero line. (c) Reconstruction of the GDF beneath the Ribbon; green shows the original surrounding GDF, orange shows the scaled GDF (see text for details). (d) Inferred Ribbon from the original data and the reconstructed GDF. (e) Determining peak and FWHM of the inferred Ribbon. (f) Contributions of the GDF and the Ribbon fluxes scaled to 100%.

ENA fluxes in the Ribbon region can be written as

$$J_1 = J_{\mathrm{Ribbon}_1} + J_{\mathrm{GDF1}}, \tag{1}$$

where J_1 is the total measured flux by IBEX, J_{Ribbon_1} is the "pure" ribbon-only flux, and J_{GDF_1} is the GDF ENA background in the Ribbon region. This background under the ribbon is thus

$$J_{\mathrm{GDF1}} = J_1 - J_{\mathrm{Ribbon}_1}. \tag{2}$$

Differencing ENA fluxes in the ribbon region during the two time periods, and based on assumption I, we can write

$$\Delta J = J_1 - J_2, \tag{3}$$

$$\Delta J = (J_{\mathrm{Ribbon}_1} + J_{\mathrm{GDF1}}) - (J_{\mathrm{Ribbon}_2} + J_{\mathrm{GDF2}}) \tag{4}$$

$$\Delta J = J_{\mathrm{Ribbon}_1} - J_{\mathrm{Ribbon}_2}, \tag{5}$$

where $J_{\mathrm{GDF1}} \sim J_{\mathrm{GDF2}}$. Changes in the Ribbon are believed to primarily be due to the varying neutral SW flux (e.g., Schwadron et al. 2018; Zirnstein et al. 2020). Based on assumption II, the ratio between the Ribbon fluxes at two time periods is some unknown constant for each pixel within this sector. The constant, a, can be unique for each azimuthal sector.

Therefore, Equation (5) can be written separately for each Ribbon azimuthal sector as

$$\Delta J = J_{\mathrm{Ribbon}_1} - a.J_{\mathrm{Ribbon}_1} = (1 - a).J_{\mathrm{Ribbon}_1},$$

rearranging

$$J_{\mathrm{Ribbon}_1} = b.\Delta J, \tag{6}$$

where b is a constant that is estimated as

$$b = {(\langle J_1\rangle - \langle B\rangle)}\Big/{\langle \Delta J\rangle}.$$

Here, $\langle B\rangle$ is the weighted average of GDF1 on both sides of the Ribbon gap.

Using Equations (2) and (6), we can now write

$$J_{\mathrm{GDF1}} = J_1 - b.\Delta J. \tag{7}$$

Uncertainties of Equation (7) follow straight propagation of derived quantities. Thus,

$$\sigma_{J_{\mathrm{GDF1}}} = \sqrt{\sigma_{J_1}^2 + (\Delta J.\sigma_b)^2 + (b.\sigma_{\Delta J})^2}. \tag{8}$$

The presented proof-of-concept method of Ribbon separation should work up to this point. However, due to the large uncertainties in the original ENA data and because the method uses differencing and thus the propagated errors get larger, we add a reasonable scaling factor to constrain the fluctuations of the inferred background to those within the limits of the GDF outside the Ribbon boundaries. Improved temporal and spatial data from, e.g., IMAP, would eliminate the need of this scaling. Equation (8) is then scaled as follows:

$$\mathrm{Scaled}\ (J_{\mathrm{GDF1}}) = [(J_{\mathrm{GDF1}} - \min(J_{\mathrm{GDF1}}))/\Delta\ J_{\mathrm{GDF1}}].\Delta B + \min(B), \tag{9}$$

where B is GDF1 on both sides of the Ribbon gap, ΔB is its range {maximum -minimum}, and $\Delta\ J_{\mathrm{GDF1}}$ is the range of J_{GDF1}. Equation (9) represents the inferred scaled GDF underneath the Ribbon and is represented in orange in Figure 3(c). It's corresponding propagated uncertainty is

$$\sigma_{\mathrm{scaled}(J_{\mathrm{GDF1}})} = \sqrt{\left(\frac{\Delta B}{\Delta J_{\mathrm{GDF1}}}\sigma_{\Delta J_{\mathrm{GDF1}}}\right)^2 + \left(\frac{J_{\mathrm{GDF1}} - \min\{J_{\mathrm{GDF1}}\}}{\Delta J_{\mathrm{GDF1}}}\sigma_{\Delta B}\right)^2 + \left(\frac{(J_{\mathrm{GDF1}} - \min\{J_{\mathrm{GDF1}}\}).\Delta B}{\Delta J_{\mathrm{GDF1}}^2}\sigma_{\Delta J_{\mathrm{GDF1}}}\right)^2 + \left(\frac{\Delta B}{\Delta J_{\mathrm{GDF1}}}\sigma_{\min\{J_{\mathrm{GDF1}}\}}\right)^2}. \tag{10}$$

Figure 3(d) shows the total observed fluxes from period P1 in green and the reconstructed GDF in red within the Ribbon bounded region as determined by Figure 3(b). It is now possible to infer the Ribbon-only fluxes by subtracting the total Ribbon flux from the newly determined GDF level. This is shown in blue, along with the propagated uncertainties (shaded region).

This process is repeated for all azimuth sectors, excluding regions that were removed as described earlier in this section. Now that the Ribbon transverse profile is determined, we derive properties of the Ribbon-only fluxes. In particular, we determine the angular distance to its center (i.e., Ribbon radius), weighted by the flux as

$$\varphi_{\mathrm{Ribbon}} = {\textstyle\sum_i \theta_i j_i}\Big/{\textstyle\sum_i j_i}, \tag{11}$$

where j_i is the derived Ribbon flux at each azimuth angle θ_i

We also determine the Ribbon FWHM by interpolating between the points forming the Ribbon transverse profile and determining the polar angles that define the FWHM intersecting locations, as illustrated in Figure 3(e).

We estimate the uncertainties by iterating over all available points, adding 1σ to each point and redoing the calculation of Equation (11), thus determining the deviated polar angle φ_i for each iteration. The uncertainty is then estimated as

$$\sigma_{\varphi_{\mathrm{Ribbon}}} = \sqrt{\sum_i (\varphi_i - \varphi_{\mathrm{Ribbon}})^2}. \tag{12}$$

The same approach is followed for the FWHM uncertainty estimation.

3. Results

Results separating the Ribbon versus GDF contribution are illustrated in Figure 3(f) where we determine the normalized contribution of the GDF-only and Ribbon-only fluxes to the

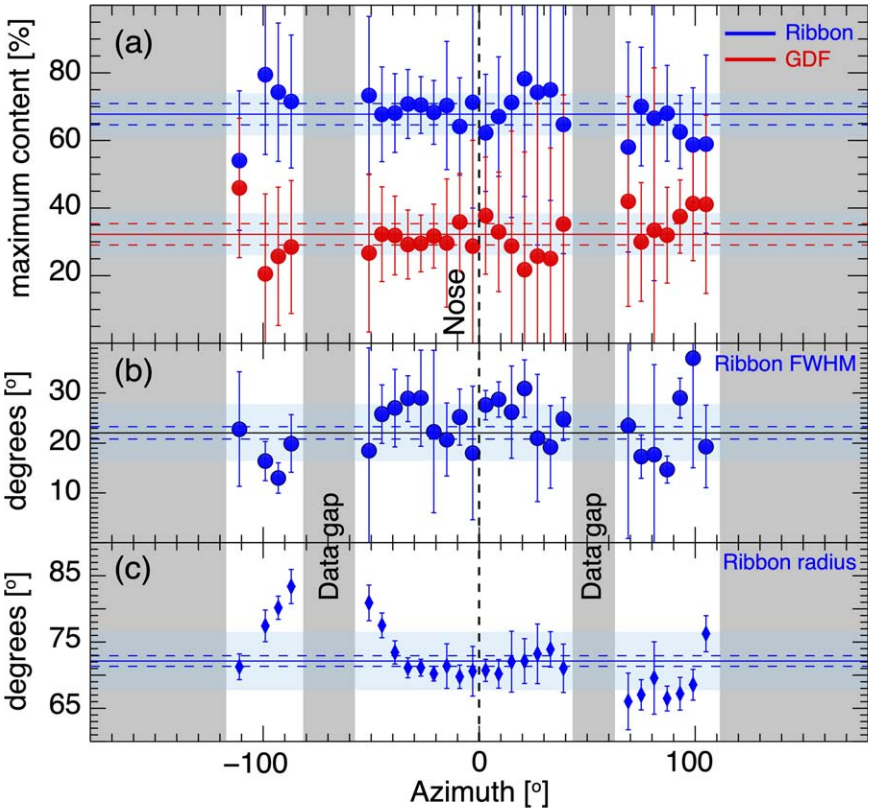

Figure 4. (a) Maximum Ribbon and GDF contributions to the total flux content across the sky in 2009–2011, centered on the azimuth intersecting the upwind direction (nose, see Figure 1). (b) inferred Ribbon-only FWHM, and (c) weighted Ribbon radius inferred using the derived Ribbon transverse profiles.

total Ribbon flux content. Red is the percentage contribution of the GDF to the total ENA flux of P1 shown in Figure 3(a) and blue is the corresponding Ribbon-only contribution.

Figure 4 summarizes the derived Ribbon properties for all directions in the sky. Figure 4(a) shows the GDF-only contributions to the measured peak Ribbon fluxes to have a weighted mean of 32.23% ± 3.15%, leaving ∼67.76% for the Ribbon-only, in 2009–2011. Figure 4(b) shows the variations of the FWHM, and Figure 4(c) shows the radius of the derived Ribbon peak for all possible directions in the sky. Gray regions indicate data gaps due to poor statistics or in regions that contain the magnetospheric obstacle viewing and in the heliotail region, as indicated earlier. Horizontal lines represent the weighted means of each panel and the dashed lines show the associated propagated or statistical uncertainty (whichever is greater; e.g., Zirnstein et al. 2022). Shaded polygons (in sky blue) represent the standard deviation.

4. Discussion and Conclusions

We present a novel method to determine the IBEX Ribbon transverse profile by taking advantage of sequential temporal variations of ENA fluxes. The method enables separating the GDF from the total Ribbon content using differences in temporal evolution of the Ribbon and GDF sources during times of large-scale, gradual changes in the SW, such as the decline in SW dynamic pressure that typically lasts several years.

Results from this analysis show that (1) The Ribbon fluxes evolve with time at different rates in different directions of the sky (Figure 2). Reasons of these variations could be a combination of different physical processes, including (i) variations in the progenitor source of the pickup ion distributions; (ii) variations in the Ribbon ENAs measured at 1 au due to changes in the heliospheric or ISMF draping geometry, and (iii) variations due to changes in the neutral SW flux in different directions of the sky (e.g., latitudinal dependence). (2) Ribbon transverse profile appears to be distinctive for different directions in the sky, and appears to have skewness- and kurtosis-like behavior in its transverse profile. Skewness of the Ribbon is possibly an indication of the spatial retention of ions outside the heliopause (Zirnstein et al. 2019). Gradual differences in the Ribbon transverse profile as a function of azimuth are expected from Ribbon models due to the ISMF draping around the heliosphere, but sharp differences could be a result of a physical process that is related to the geometry of the Ribbon around the heliopause or a nonuniform scattering environment for the source ions along the Ribbon. (3) Maximum Ribbon-only flux contributions across the sky are on the order of ∼68%, while the GDF accounts for the remaining ∼32%, in 2009–2011 (Figure 4(a)). These values make the Ribbon effectively ∼2 factor higher than the surrounding GDF near the peak. (4) The Ribbon peak location and radius at ∼1.1 keV during the studied time period are $\sim 22^{\circ}\!.07 \pm 1^{\circ}\!.24$ and $\sim 72^{\circ}\!.13^{\mathrm{o}} \pm 0^{\circ}\!.79$, respectively (Figure 4(c)). The radius agrees well with the earlier studies of Ribbon analysis (Fuselier et al. 2009; Funsten et al. 2013; Dayeh et al. 2019).

Note that the course resolution of IBEX data prevents a more precise determination of the Ribbon geometrical properties without fitting a function directly to the Ribbon flux, which was intentionally avoided in this paper. Furthermore, the shape of the heliosphere and the way that the ISMF is wrapped around it inherently affects the distance to the Ribbon source, both in terms of the inner versus outer edge of the transverse profile measured by IBEX, as well as parts of the Ribbon closer to the nose (e.g., Figure 3 in Zirnstein et al. 2019). Because of this, same-energy ENAs from different distances along and across the Ribbon experience different delays arriving at IBEX (e.g., near-nose versus high latitudes versus inner/outer edge). The time difference between P1 and P2 in this study partially accounts for this, but it is an effect that should be accounted for when improved observations are available.

The evolution of the Ribbon is highly variable and appears in some cases to be symmetric around its peak or right and left skewed, have a variable peak sharpness, or have an irregular bumpy-like transverse profile. The latter case makes it very complex to analyze because the Ribbon fluctuations appear as part of the enhanced background and it is impossible to perform such a separation using this method only. About four azimuthal directions in the sky exhibit this property and are thus excluded from the analysis. The GDF variability also introduces additional randomness to these variations. Taken together, these reasons provide intrinsic limitations of this method to infer the Ribbon transverse profile along some directions of the sky.

In summary, we present a new method to potentially infer the Ribbon transverse profile and separate the Ribbon ENA fluxes from the underlying GDF by using temporal variations rather than spatial variations. Our methodology does not rely on interpolating across the Ribbon, but does require a few assumptions about how the Ribbon's transverse profile should change over time compared to the GDF. We derive an average Ribbon radius of ∼72°.1, which is close to the derived values of Dayeh et al. (2019; ∼74°.8) and Funsten et al. (2013; 74°.5), whose difference may be due to the fact that the previous analyses used Gaussian fitting to find the ribbon peak distance from the center, while we use the weighted mean of the ribbon flux. Nevertheless, comparison of this method with other separation methods is a topic for a future study and is beyond the scope of this paper. Moreover, this method may only work for measurements of the Ribbon near ∼1 keV, which responds strongest to changes in the neutral SW flux and overlaps the peak GDF enhancement near the nose of the heliosphere. The method should work better at higher angular resolutions during times of gradual evolution in solar activity and thus presents a timely proof of concept for analyzing anticipated IMAP ENA measurements. IMAP will cover a broader ENA energy range with a higher spatial resolution, and thus enables a better understanding of the Ribbon processes and evolution, in both time and space.

This work was carried out as part of the IBEX mission, which is part of NASA's Explorer program. Authors M.A.D. and E.J.Z. acknowledge support from NASA grants 80NSSC17K0597 and 80NSSC20K0783.

ORCID iDs

M. A. Dayeh https://orcid.org/0000-0001-9323-1200
E. J. Zirnstein https://orcid.org/0000-0001-7240-0618
D. J. McComas https://orcid.org/0000-0001-6160-1158

References

Dayeh, M. A., Fuselier, S. A., Funsten, H. O., et al. 2015, GeoRL, 42, 2115
Dayeh, M. A., Zirnstein, E. J., Desai, M. I., et al. 2019, ApJ, 879, 84
Dayeh, M. A., Zirnstein, E. J., Fuselier, A. A., et al. 2022, ApJS, 261, 27
Funsten, H. O., Allegrini, F., Crew, G. B., et al. 2009, Sci, 326, 964
Funsten, H. O., Bzowski, M., Cai, D. M., et al. 2015, ApJ, 799, 68
Funsten, H. O., DeMajistre, R., Frisch, P. C., et al. 2013, ApJ, 776, 30
Fuselier, S. A., Allegrini, F., Funsten, H. O., et al. 2009, Sci, 326, 962
Giacalone, J., & Jokipii, J. R. 2015, ApJL, 812, L9
Heerikhuisen, J., Pogorelov, N. V., Zank, G. P., et al. 2010, ApJL, 708, L126
Izmodenov, V. V., Malama, Y. G., Ruderman, M. S., et al. 2009, SSRv, 146, 329
McComas, D. J., Allegrini, F., Bochsler, P., et al. 2009a, SSRv, 146, 11
McComas, D. J., Allegrini, F., Bochsler, P., et al. 2009b, Sci, 326, 959
McComas, D. J., Bzowski, M., Dayeh, M. A., et al. 2020, ApJS, 248, 26
McComas, D. J., Christian, E. R., Schwadron, N. A., et al. 2018b, SSRv, 214, 116
McComas, D. J., Dayeh, M. A., Funsten, H. O., Livadiotis, G., & Schwadron, N. A. 2013, ApJ, 771, 77
McComas, D. J., Dayeh, M. A., Funsten, H. O., et al. 2018a, ApJL , 856, L10
McComas, D. J., Dayeh, M. A., Funsten, H. O., et al. 2019, ApJ, 872, 127
McComas, D. J., Ebert, R. W., Elliot, H. A., et al. 2008, GRL, 35, L18103
McComas, D. J., Lewis, W. S., & Schwadron, N. A. 2014, RvGeo, 52, 118
McComas, D. J., Zirnstein, E. J., Bzowski, M., et al. 2017, ApJS, 229, 41
Möbius, E., Liu, K., Funsten, H., Gary, S. P., & Winske, D. 2013, ApJ, 766, 129
Opher, M., Prested, C., McComas, D. J., et al. 2013, ApJL, 776, L32
Reisenfeld, D. B., Bzowski, M., Funsten, H. O., et al. 2021, ApJS, 254, 40
Schwadron, N. A., Allegrini, F., Bzowski, M., et al. 2011, ApJS, 731, 56
Schwadron, N. A., Allegrini, F., Bzowski, M., et al. 2018, ApJS, 239, 1
Schwadron, N. A., Bzowski, M., Crew, G. B., et al. 2009, Sci, 326, 966
Schwadron, N. A., & McComas, D. J. 2013, ApJ, 764, 92
Schwadron, N. A., & McComas, D. J. 2019, ApJ, 887, 247
Schwadron, N. A., Moebius, E., Fuselier, S. A., et al. 2014, ApJS, 215, 13
Swaczyna, P., Bzowski, M., & Sokół, J. M. 2016, ApJ, 827, 71
Swaczyna, P., Eddy, T. J., Zirnstein, E. J., et al. 2022, ApJS, 258, 6
Swaczyna, P., McComas, D. J., Zirnstein, E. J., & Heerikhuisen, J. 2019, ApJ, 887, 223
Zirnstein, E. J., Dayeh, M. A., Heerikhuisen, J., McComas, D. J., & Swaczyna, P. 2021, ApJS, 252, 26
Zirnstein, E. J., Dayeh, M. A., McComas, D. J., & Sokół, J. M. 2017, ApJ, 846, 63
Zirnstein, E. J., Funsten, H. O., Heerikhuisen, J., & McComas, D. J. 2016a, A&A, 586, A31
Zirnstein, E. J., Heerikhuisen, J., Funsten, H. O., et al. 2016b, ApJL, 818, L18
Zirnstein, E. J., Heerikhuisen, J., & McComas, D. J. 2015, ApJL, 804, L22
Zirnstein, E. J., Heerikhuisen, J., Zank, G. P., et al. 2014, ApJ, 783, 129
Zirnstein, E. J., Kim, T. K., Mostafavi, P., et al. 2020, ApJ, 891, 56
Zirnstein, E. J., Shrestha, B. L., McComas, D. J., et al. 2022, NatAs, 6, 1398
Zirnstein, E. J., Swaczyna, P., McComas, D. J., Heerikhuisen, J., et al. 2019, ApJ, 879, 106